AIAA JOURNAL
Vol. 55, No. 7, July 2017

Machine-Learning-Augmented Predictive Modeling of Turbulent Separated Flows over Airfoils

Anand Pratap Singh*
University of Michigan, Ann Arbor, Michigan 48104
Shivaji Medida†
Altair Engineering, Inc., Sunnyvale, California 94086
and
Karthik Duraisamy‡
University of Michigan, Ann Arbor, Michigan 48104

DOI: 10.2514/1.J055595

A modeling paradigm is developed to augment predictive models of turbulence by effectively using limited data generated from physical experiments. The key components of the current approach involve inverse modeling to infer the spatial distribution of model discrepancies and machine learning to reconstruct discrepancy information from a large number of inverse problems into corrective model forms. The methodology is applied to turbulent flows over airfoils involving flow separation. Model augmentations are developed for the Spalart–Allmaras model using adjoint-based full-field inference on experimentally measured lift coefficient data. When these model forms are reconstructed using neural networks and embedded within a standard solver, it is shown that much improved predictions in lift can be obtained for geometries and flow conditions that were not used to train the model. The neural-network-augmented Spalart–Allmaras model also predicts surface pressures extremely well. Portability of this approach is demonstrated by confirming that predictive improvements are preserved when the augmentation is embedded in a different commercial, finite element solver. The broader vision is that, by incorporating data that can reveal the form of the innate model discrepancy, the applicability of data-driven turbulence models can be extended to more general flows.

I. Introduction

THE accurate modeling and simulation of turbulent flows are critical to several applications in engineering and physics. From the viewpoint of affordability, turbulence closure models [either in Reynolds-averaged Navier–Stokes (RANS) form or in a near-wall context in an eddy-resolving model] will continue to be indispensable for the foreseeable future [1]. Existing turbulence closures have proven to be quite useful in many contexts, but it is well-recognized that complex effects such as flow separation, secondary flows, etc., are poorly modeled.

Although new and increasingly complex models are being developed [2–4] and demonstrated to be accurate in some problems, it can be argued that there has not been a significant improvement in predictive accuracy over the past 15 years. As a result, the majority of the RANS models that are used in both industrial and academic computational fluid dynamics (CFD) solvers were initially developed and published in the 1990s. A critical issue in turbulence model development is that even the most sophisticated model invokes radically simplifying assumptions about the structure of the underlying turbulence. Thus, the process of developing a practical turbulence model combines physical intuition, empiricism, and engineering judgment while constrained by robustness and cost considerations. As a result, even if a model is based on a physically and mathematically appealing idea (for example, elliptic relaxation [5,6]), the model formulation typically devolves into the calibration of a large number of free parameters or functions using a small set of canonical problems.

Against this scenario, our ability to perform detailed high-fidelity computations and resolved measurements has improved dramatically over the past decade. At the same time, data science is on the rise because of improvements in computational power and the increased availability of large datasets. This has been accompanied by significant improvements in the effectiveness and scalability of data analytics and machine-learning techniques. Given these advances, we believe that data-driven modeling and machine learning will play a critical role in improving the understanding and modeling of turbulence.

In the study of turbulent flows, machine-learning techniques appear to have first been used to recreate the behavior of near-wall structures in a turbulent channel flow [7] and to extract coherent spatiotemporal structures [8]. With a view toward quantifying model errors, several researchers [9–12] have used experimental data to infer model parameters. Cheung et al. [13,14] employed Bayesian model averaging [15] to calibrate model coefficients. Edeling et al. [11] used statistical inference on skin-friction and velocity data from a number of boundary-layer experiments to quantify the parametric model error. These methods provide insight into parametric uncertainties and address some of the deficiencies of a priori processing of data.

Dow and Wang [16,17] made progress toward addressing nonparametric uncertainties by inferring the spatial structure of the discrepancy in the eddy viscosity coefficient based on a library of direct numerical simulation (DNS) datasets. The discrepancy between the inferred and modeled eddy viscosity was represented as a Gaussian random field and propagated to obtain uncertainty bounds on the mean flow velocities.

Emory et al. [18], Gorle et al. [19], and Emory et al. [20] introduced ad hoc but realizable perturbations to the nondimensional Reynolds stress anisotropy tensor a_{ij} to quantify structural errors in eddy viscosity models. Tracey et al. [21] applied neural networks to large-eddy simulation data to learn the functional form of the discrepancy in the eigenvalues of a_{ij} and injected these functional forms in a predictive simulation in an attempt to obtain improved predictions. Xiao et al. [22] inferred the spatial distribution of the perturbations in a_{ij} and turbulent kinetic energy by assimilating DNS data. Weatheritt [23] used evolutionary algorithms on DNS data to construct nonlinear stress–strain relationships for RANS models.

Ling and Templeton [24] used machine-learning-based classifiers to ascertain regions of the flow in which commonly used assumptions

Received 22 August 2016; revision received 7 January 2017; accepted for publication 23 January 2017; published online 9 May 2017.

*Ph.D. Candidate, Department of Aerospace Engineering.
†Solver Development Manager, AcuSolve.
‡Associate Professor, Department of Aerospace Engineering.

break down. King et al. [25] formulated a damped least-squares problem at the test-filter scale to obtain coefficients of a subgrid-scale model. In both of these works, results were demonstrated in an a priori setting.

Duraisamy et al. [26], Tracey et al. [27], Parish et al. [28], and Singh and Duraisamy [29] took the first steps toward improving predictive model forms by defining a data-driven modeling paradigm based on field inversion and machine learning (FIML). The FIML approach consists of three key steps: 1) inferring the spatial (nonparametric) distribution of the model discrepancy in a number of problems using Bayesian inversion, 2) transforming the spatial distribution into a functional form (of model variables) using machine learning, and 3) embedding the functional form in a predictive setting. Predictions were demonstrated in turbulent channel flows and transitional flows with imposed pressure gradients. Note that steps 1 and 2 involve offline (training) computations, whereas step 3 is online (prediction). Ling et al. [30,31] and Wang et al. [32] bypassed the inference step and used machine learning directly on DNS data to obtain a more comprehensive model (compared to Tracey et al. [21]) for the anisotropy tensor a_{ij}. Ling et al. [30] used neural networks to reconstruct a_{ij} and propagate the model to velocity field predictions. Wang et al. [32] used random forests to inject the model correction as a one-time postprocessing step to a computed baseline solution.

In this work, we extend the paradigm of data-driven modeling to assist in the development of turbulence models and predictive simulation of turbulent flow over airfoils. In particular, we demonstrate the ability of inverse modeling to provide quantitative modeling information based on very limited experimental data and the use of machine learning to reconstruct this information into corrective model forms. When these model forms are embedded within a standard solver setting, it is shown that significantly improved predictions can be achieved.

II. Problem and Approach

Turbulent flow separation over lifting surfaces is critical to many applications, including high-lift systems, offdesign operating envelope of new vehicles, airframe noise, wind turbines, turbomachinery flows, and combustors. A RANS turbulence modeling capability that can confidently predict separated flows in these various contexts would be a key enabling factor in the development of aerospace and energy systems of the future. The ability to accurately model the effects of strong adverse pressure gradients (APGs) is crucial to the prediction of boundary-layer separation in wall-bounded flows; however, most one- and two-equation RANS turbulence models fail to accurately predict stall onset for airfoils at high angles of attack, where strong APGs are encountered. Consequently, they tend to overpredict the maximum lift and stall onset angle for a given set of flow conditions.

Celic and Hirschel [33] compared the performance of 11 eddy-viscosity-based turbulence models for aerodynamic flows with APGs and concluded that none of the models performed satisfactorily for flow past airfoils near maximum lift conditions. This deficiency can be attributed to the underlying assumptions and simplifications that are part of all eddy-viscosity-based turbulence models. One such assumption implies a balance between the production and dissipation of turbulent kinetic energy. This assumption allows for the scaling of velocity profiles in the defect layer, and it is instrumental in the formulation of many turbulence models. However, it is well known that practical boundary layers under strong APGs are not in equilibrium. In addition, the outer layer scaling is affected by the APG, whereas the viscous sublayer and log layer are relatively unchanged. Many turbulence models that assume equilibrium conditions fail to produce satisfactory behavior for strong APG flows. Certain models with stress limiters, such as the shear-stress transport version of the k–ω turbulence model [34], Wilcox's modified k–ω [35] model, and the strain-adaptive formulation of the Spalart–Allmaras turbulence model [36,37], are known to perform slightly better than the other models. Although using more sophisticated turbulence models (nonlinear eddy viscosity models, second moment closure models, etc.) might produce better results, poor robustness and higher computational costs associated with the usage of these methods are major deterrents to their wider applicability for practical flows. These models are still calibrated using information from canonical configurations and applied in situations dissimilar to those in which calibrations were made. In the present work, more realistic flows are used to guide model development.

As proof of concept for the feasibility of data-assisted modeling, Tracey et al. [27] applied machine learning to a database of solutions of a known turbulence model. The known turbulence model was considered to be the surrogate truth. These solutions primarily involved flat plates and airfoils. A deficient turbulent model (with deliberately removed source terms) was then augmented with these machine-learned functional forms. This augmented turbulence model was able to accurately reproduce radically different flows such as transonic flow over a wing. Although it was relatively easy to make a priori (and one-time) evaluations of the trained model, key lessons were learned about the formulation of the learning problem because the neural network (NN) (artificial neural network) had to be evaluated and injected during every iteration of a converging partial differential equation solver.

The aforementioned work demonstrated that, if the underlying model form was discoverable and the data were comprehensive enough, a machine-learning technique such as an artificial neural network could adequately describe it. The challenge in predictive modeling, however, is to extract an optimal model form that is sufficiently accurate. Constructing such a model and demonstrating its predictive capabilities for a class of problems is the objective of this work. This data-driven framework is specifically demonstrated in predictions of turbulent, separated flows over airfoils.

A schematic of the approach is provided in Fig. 1. Various aspects of the schematic are organized in the paper as follows: Section III introduces the inversion framework that uses limited experimental data G_{exp} to generate fields of modeling information $\beta(\boldsymbol{x})$ that account for the model discrepancy. Section IV introduces the role of machine learning in transforming information from a number of inverse problems $\beta^j(\boldsymbol{x})$ into model forms $\beta(\boldsymbol{\eta})$, where $\boldsymbol{\eta}$ represents local field variables available in the model. Section V demonstrates that embedding model corrections β during the simulation process can improve predictive capabilities. Section VI presents a summary of this work and perspectives on the extension of these techniques to general turbulence modeling.

Discretization: The flow solver ADTURNS [38–40] is based on a cell-centered finite volume formulation of the compressible RANS equations on structured grids. The inviscid fluxes are discretized using the third-order MUSCL scheme [41] in combination with the

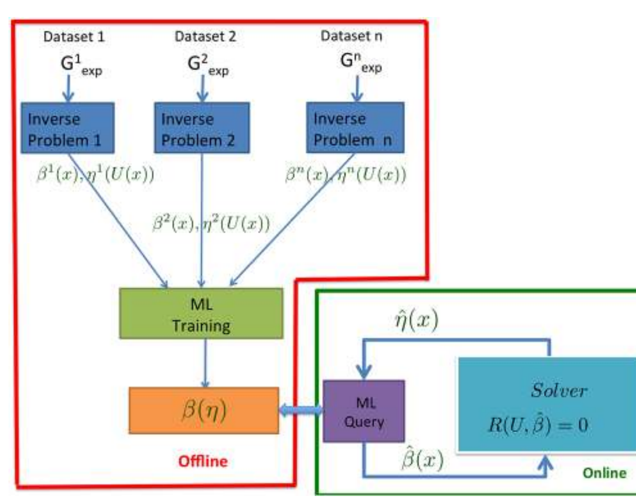

Fig. 1 Schematic of field inversion and machine-learning framework for data-augmented turbulence modeling.

approximate Riemann solver of Roe [42]. The diffusive contributions are evaluated using a second-order-accurate central differencing scheme. Implicit operators are constructed using the diagonalized alternating direction implicit scheme [43].

For the computations, the flow domain over airfoils is discretized using a C grid with 291 points in the wraparound direction and 111 points in the wall-normal direction. At this resolution, which corresponds to 200 grid points on the airfoil surface, numerical errors are low enough to not obscure the treatment of turbulence modeling errors. This was verified by performing a grid-convergence study. The far-field boundaries are located 35 chord lengths from the airfoil surface. Characteristic freestream boundary conditions are used for the flow variables at the far field, and the eddy viscosity is set to the fully turbulent value.

The field inversion procedure requires gradients with respect to every grid point. These gradients are most effectively determined using a discrete adjoint approach [44]. The required derivatives are computed as detailed in Appendix A.

III. Field Inversion

Our philosophy of inferring and reconstructing one or more corrective functional forms is generally in scope with regard to data-driven modeling [28,29]. Although the methodology is applicable to both eddy viscosity and Reynolds stress models, the focus of the present work is restricted to the Spalart–Allmaras (SA) model [37] (refer to Appendix B for detailed formulation). The baseline SA model can be written as

$$\frac{\mathrm{D}\tilde{\nu}}{\mathrm{D}t} = P(\tilde{\nu}, \boldsymbol{U}) - D(\tilde{\nu}, \boldsymbol{U}) + T(\tilde{\nu}, \boldsymbol{U}) \tag{1}$$

where $\boldsymbol{U}$ represents the Reynolds averaged conserved flow variables; and $P(\tilde{\nu}, \boldsymbol{U})$, $D(\tilde{\nu}, \boldsymbol{U})$, and $T(\tilde{\nu}, \boldsymbol{U})$ represent the production, destruction, and transport terms, respectively. The preceding equation is used with a nonlinear functional relationship to derive an eddy viscosity ν_t from $\tilde{\nu}$, which is then used in a Boussinesq formulation to close the RANS equations. The major source of modeling deficiency is the structural form of the model rather than parameters within the imposed model form. Thus, benefits from classical parameter estimation will be limited. In other words, the functional forms of the terms in Eq. (1) are themselves inaccurate, and they require a reformulation.

The goal, then, is to construct generalizable functional corrections to the model form in Eq. (1). Accordingly, a spatially varying term $\beta(\boldsymbol{x})$ is introduced as a multiplier of the production term $P(\tilde{\nu}, \boldsymbol{U})$:

$$\frac{\mathrm{D}\tilde{\nu}}{\mathrm{D}t} = \beta(\boldsymbol{x})P(\tilde{\nu}, \boldsymbol{U}) - D(\tilde{\nu}, \boldsymbol{U}) + T(\tilde{\nu}, \boldsymbol{U}) \tag{2}$$

It must be recognized that the introduction of $\beta(\boldsymbol{x})$ changes the entire balance of the model (and need not be interpreted as merely a modification of the production term). It is equivalent to adding a source term $\boldsymbol{\delta}(\boldsymbol{x}) = (\beta(\boldsymbol{x}) - 1)P(\boldsymbol{x})$. Inferring β, however, leads to a better conditioned inverse problem, as β is nondimensional and has a simple initial value of unity.

Assume a flow configuration (with a particular geometry, angle of attack, Reynolds number, etc.) consisting of N_m control volumes. Given N_d data points (such as wall pressure, skin friction, etc.) $G_{j,\mathrm{exp}}$, we define the following inverse problem to extract the optimal field $\beta \equiv \beta(x_n)$: $1 \leq n \leq N_m$:

$$\min_{\beta} \sum_{j=1}^{N_d} [G_{j,\mathrm{exp}} - G_j(\beta)]^2 + \lambda \sum_{n=1}^{N_m} [\beta(x_n) - 1]^2 \tag{3}$$

where $G_j(\beta)$ is the output of the RANS model. This inverse problem is most straightforwardly interpreted in a classical frequentist sense with Tikhonov regularization [45], or loosely as the maximum a posteriori estimate in a Bayesian setting assuming Gaussian distributions and a prior of unity. In the former setting, λ is a regularization constant; in the latter, it represents the ratio of the observational covariance to the prior covariance.[§] It is to be noted that, in the context of this work, the solution of a large number of inverse problems is used as a means to define corrective functions. Thus, finer-grained interpretations or formulations of the inverse problem and treatment of uncertainties, although important, are not of a primary concern in this work. A more formal treatment of observational errors and prior confidence has been pursued in previous work [28], but application was restricted to simpler problems.

Nevertheless, an optimal value of β is sought at every discrete location in the computational domain and used in Eq. (2), conjoined with the conservation equations for the ensemble-averaged mass, momentum, and energy. The resulting inverse problem is extremely high-dimensional, and an efficient adjoint-based optimization framework is employed. For further details, please refer to Appendix A.

If experimental surface pressure coefficients C_p are used as data points [29], the following minimization problem is formulated:

$$\min_{\beta} \left[\sum_{j=1}^{N_d} \left[C_{p_{j,\mathrm{exp}}} - C_{p_j}(\beta) \right]^2 + \lambda \sum_{n=1}^{N_m} [\beta(x_n) - 1]^2 \right] \tag{4}$$

However, in the majority of experimental tests of flow over airfoils, the surface pressure is not measured. Therefore, we use the lift coefficient C_l as the observational data. Thus, the following optimization problem is formulated:

$$\min_{\beta} \left[[C_{l,\mathrm{exp}} - C_l(\beta)]^2 + \lambda \sum_{n=1}^{N_m} [\beta(x_n) - 1]^2 \right] \tag{5}$$

The two objective functions [Eqs. (4) and (5)] were confirmed to lead to a similar solution to the inverse problem (Fig. 2). Although there are discrepancies in the poststall region, the near-wall features in $\beta(\boldsymbol{x})$ are almost identical, resulting in indistinguishable surface pressures. The entire set of inverse problems in this work is solved for the lift-based objective function [Eq. (5)] with $\lambda = 4 \times 10^{-4}$. This implies a much higher level of confidence in the experimentally measured lift compared to the variability of β. The optimal solution was indeed confirmed to be insensitive to order-of-magnitude variations in λ.

To further probe the validity of using pressure-based information for field inversion, Appendix C presents an example in which the Reynolds stress field is available. Additional information on the characteristics of the inversion procedure can be found in [29].

In Sec. V, the ability of the lift-based model correction to accurately predict surface pressures will be further demonstrated. The ability to use only the lift coefficient to generate modeling information greatly enhances the applicability of the current framework to assimilate a vast amount of available data.

The inverse solution serves as an input to the machine-learning algorithm while providing qualitative and quantitative insight to the modeler. It is known that eddy-viscosity-based turbulence models generate very high levels of turbulence at high angles of attack, resulting in delayed separation and stall [46]. The inverse solution adjusts for this deficiency by reducing the generation of turbulence in the near-wall preseparation region, i.e., the $\beta(\boldsymbol{x}) < 1$ region in Fig. 3. This reduced production results in early flow separation, which can be observed in the wall shear stress (Fig. 4a). Furthermore, Fig. 4b reinforces the fact that a complex relationship exists between the model corrections and the pressure gradient parameter[¶]:

$$\Pi = \frac{\delta^*}{\tau_w} \frac{\mathrm{d}P}{\mathrm{d}s}$$

[§]This assumes that the covariance matrices are Gaussian and diagonal.

[¶]Note that δ is the displacement thickness of the boundary layer and $\mathrm{d}P/\mathrm{d}s$ is the pressure gradient.

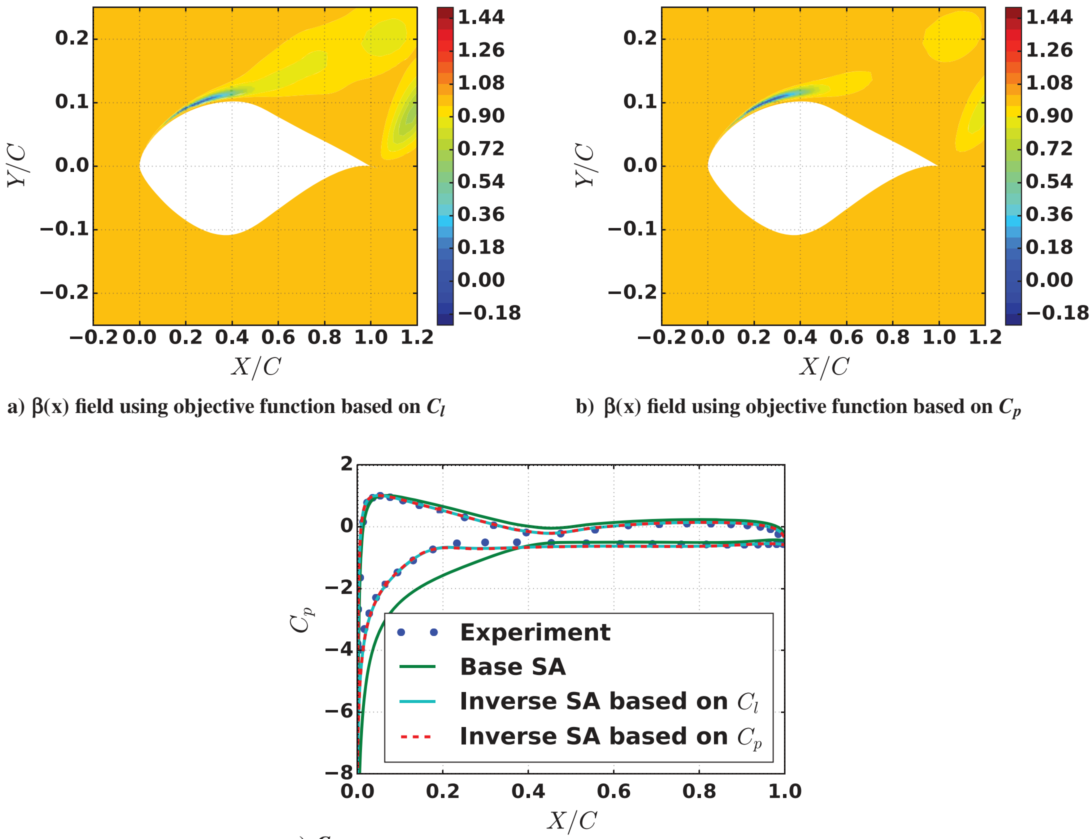

a) β(x) field using objective function based on C_l

b) β(x) field using objective function based on C_p

c) C_p

Fig. 2 Inverse solutions using objective function based on lift and surface pressure coefficients.

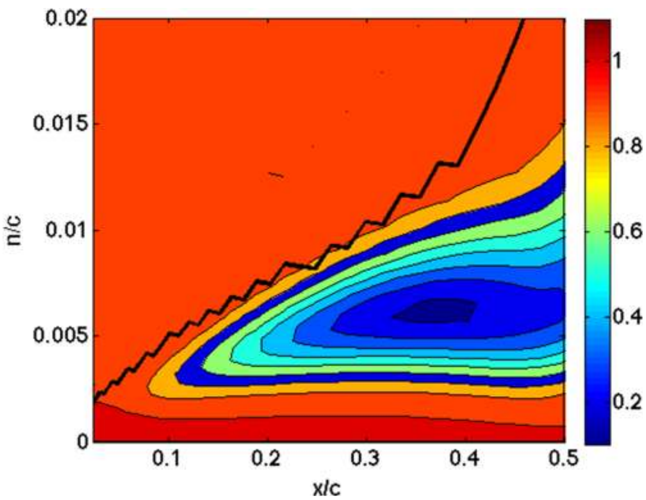

Fig. 3 β_{inverse} for a representative airfoil. n/c is the normalized distance from the airfoil surface.

IV. Machine Learning

The inverse approach presented in the previous section results in an optimal correction field for a given flow condition and geometry. To be useful in predictive modeling, the problem-specific information encoded in $\beta(\boldsymbol{x})$ must be transformed into modeling knowledge [28]. This is done by extracting the functional relationship $\beta(\boldsymbol{x}) \approx \beta(\boldsymbol{\eta})$, where $\boldsymbol{\eta} = [\eta_1, \eta_2, \ldots, \eta_M]^T$ are input features derived from mean-field variables that will be available during the predictive solution process. The functional relationship must be developed by considering the output of a number of inverse problems representative of the modeling deficiencies relevant to the predictive problem. Furthermore, as will be explained in the following, elements of the feature vector $\boldsymbol{\eta}$ are chosen to be locally nondimensional quantities such that the functional relationship $\beta(\eta)$ is useful for different problems in which the $\boldsymbol{\eta}$ variables are realizable.

A. Features

To build a set of features $\boldsymbol{\eta}$ upon which the functional relationship $\beta(\boldsymbol{\eta})$ will be based, a logical place to start would be to identify the independent variables in the baseline SA model. The source terms in the SA model are a function of four local flow quantities ν, $\hat{\nu}$, Ω, and d, which represent the kinematic viscosity, the SA working variable, the vorticity magnitude, and the distance from the wall, respectively. As discussed in [27], these quantities do not constitute an appropriate choice for the input feature vector to the machine-learning algorithm. They are dimensional quantities that may have different numeric values even when two flows are dynamically similar. Thus, the inputs are rescaled [27] by relevant local quantities that are representative of the state of turbulence. An obvious locally nondimensional quantity in the baseline SA model is $\chi = \hat{\nu}/\nu$. We define local scales, $\nu + \hat{\nu}$ and d, and introduce an additional variable:

$$\bar{\Omega} = \frac{d^2}{\hat{\nu} + \nu}\Omega \tag{6}$$

With these definitions, the nondimensional versions $(\bar{P}, \bar{D})$ of the existing production and destruction terms (P, D) are given by the following:

$$\bar{P} = \frac{d^2}{(\hat{\nu} + \nu)^2} s_p = c_{b1}(1 - f_{t2})\left(\frac{\chi}{\chi + 1}\right)\left(\bar{\Omega} + \frac{1}{\kappa^2}\frac{\chi}{\chi + 1} f_{t2}\right)$$
$$\bar{D} = \frac{d^2}{(\hat{\nu} + \nu)^2} s_d = \left(\frac{\chi}{\chi + 1}\right)^2 c_{w1} f_w$$

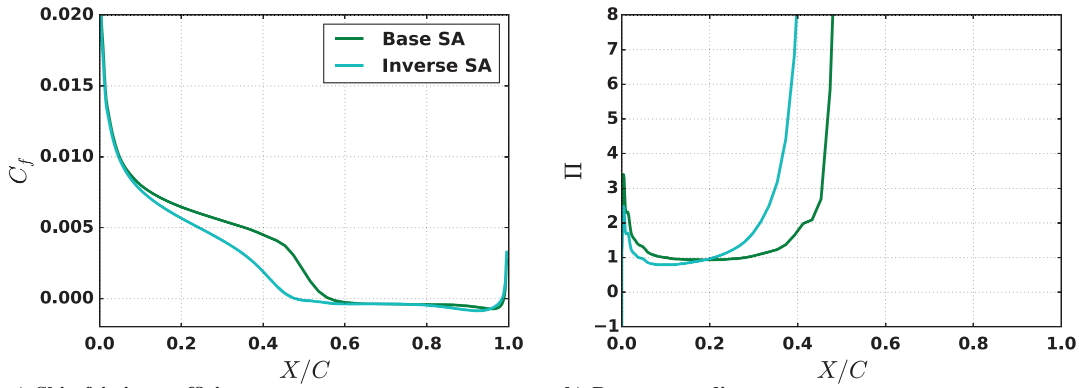

a) Skin-friction coefficient b) Pressure gradient parameter

Fig. 4 Prior and posterior quantities for the case in Fig. 3.

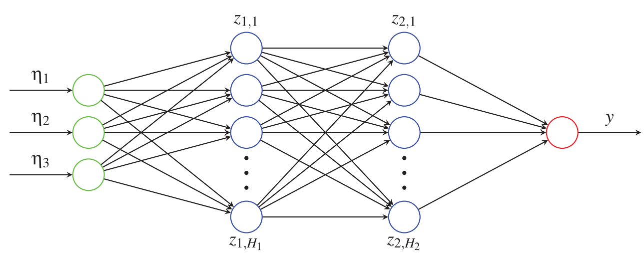

Fig. 5 Network diagram for a feedforward NN with three inputs, two hidden layers, and one output.

where c_{b1} and c_{w1} are constants, f_{t2} is a function of χ, and f_w is a function of $\bar{\Omega}$ and χ. Thus, the locally nondimensionalized source terms in the baseline SA model are dependent only on $\bar{\Omega}$ and χ.

The set of features that was evaluated includes

$$\left\{\bar{\Omega}, \chi, S/\Omega, \tau/\tau_{\text{wall}}, P/D, f_d\right\}$$

where S, τ, τ_{wall}, and f_d represent the strain-rate magnitude, the magnitude of the Reynolds stress, the wall shear stress, and a shielding function used in detached-eddy simulation [47], respectively.

B. Neural Networks

In previous work, supervised learning techniques were experimented with [48], including single-/multiscale Gaussian process regression [49] and artificial neural networks [50]. In this work, we pursue NNs because of their efficiency because they can be evaluated at a computational cost that is independent of the size of the training data. (We also appreciate that other techniques such as support vector and polynomial regressors can be as scalable as NNs; thus, the choice of NNs is based on prior experience rather than on objective considerations.)

The standard NN algorithm operates by constructing linear combinations of inputs and transforming them through nonlinear activation functions. The process is repeated once for each hidden layer (marked in blue in Fig. 5) in the network until the output layer is reached. Figure 5 presents a sample NN. For this sample network, the values of hidden nodes $z_{1,1}$ through z_{1,H_1} would be constructed as

$$z_{1,j} = a_{(1)}\left(\sum_{i=1}^{3} w_{ij}^{(1)} \eta_i\right) \tag{7}$$

where $a_{(1)}$ and $w_{ij}^{(1)}$ are the activation function and weights associated with the first hidden layer, respectively. Similarly, the second layer of hidden nodes is constructed as

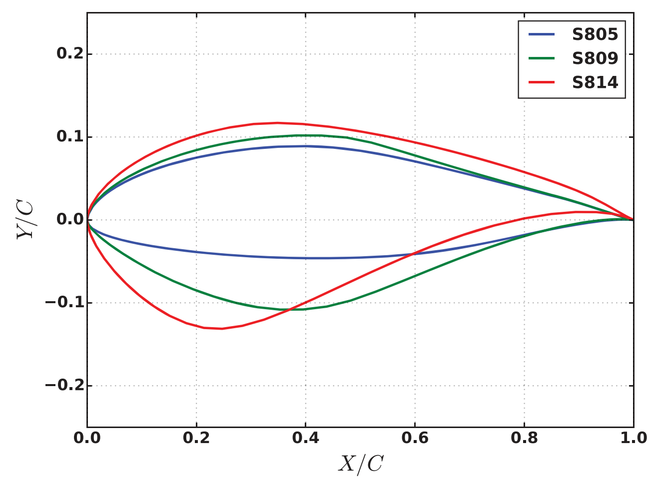

Fig. 6 Three different airfoils used for training and testing the neural network model. Note that axes are scaled differently.

$$z_{2,j} = a_{(2)}\left(\sum_{i=1}^{H_1} w_{ij}^{(2)} z_{1,i}\right) \tag{8}$$

Finally, the output is

$$y \approx f(\boldsymbol{\eta}) = a_{(3)}\left(\sum_{i=1}^{H_2} w_{ij}^{(3)} z_{2,i}\right) \tag{9}$$

Given training data, error backpropagation algorithms [50] are used to find $w_{ij}^{(n)}$.

Once the weights are found, computing the output depends only on the number of hidden nodes and not on the volume of the training data. Hyperparameters of the NN method include the number of hidden layers, the number of nodes in each hidden layer, and the forms of the activation functions.

The Fast Artificial Neural Network Library [51] is used for this work. This library uses resilient backpropagation (RPROP; [52]).

Table 1 Results of fivefold cross validation[a]

Fold	Training error	Validation error
1	0.9403	0.8832
2	0.9272	0.8665
2	0.9293	0.8572
2	0.9404	0.8847
2	0.9401	0.9033

[a]The error metric is the coefficients of determination R^2.

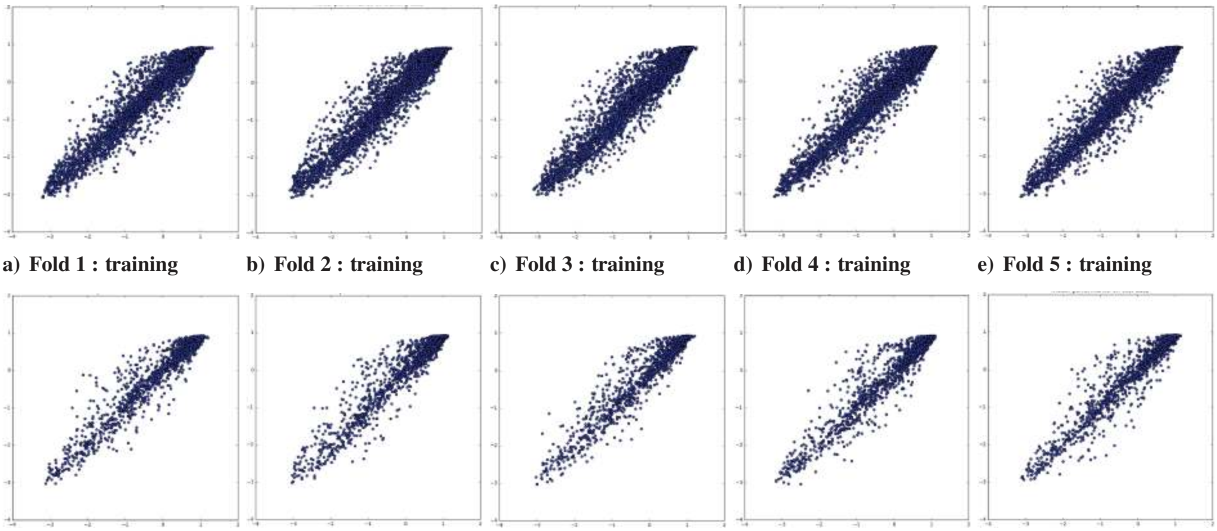

a) Fold 1 : training b) Fold 2 : training c) Fold 3 : training d) Fold 4 : training e) Fold 5 : training

f) Fold 1 : testing g) Fold 2 : testing h) Fold 3 : testing i) Fold 4 : testing j) Fold 5 : testing

Fig. 7 Neural network training on dataset P, where the x and y axes correspond to the true and predicted values, respectively.

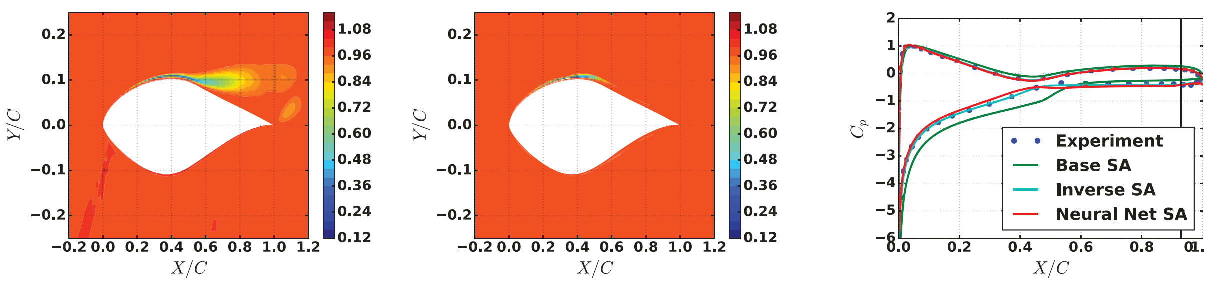

a) β (x) from inverse SA b) β (U) from NN-augmented SA (prediction) c) Pressure coefficient

Fig. 8 Comparison of inverse and NN-augmented predictions (using dataset P) for S809 airfoil at $\alpha = 14$ deg and $Re = 2 \times 10^6$.

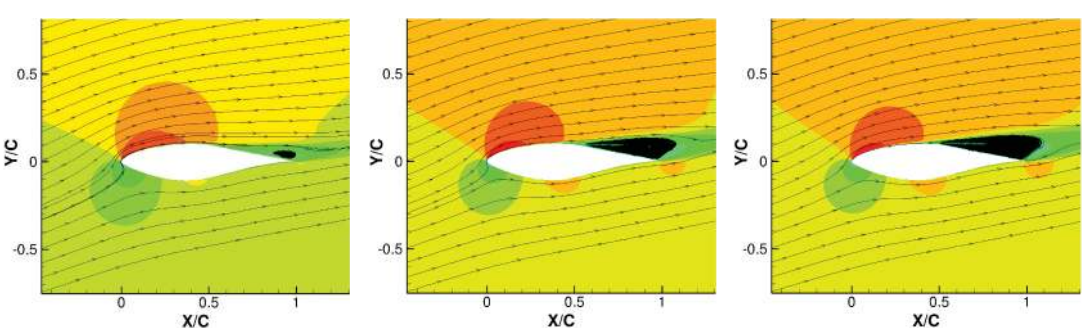

a) Base SA b) Inverse SA c) NN-augmented SA (prediction)

Fig. 9 Streamlines and X-velocity contour for S809 airfoil at $Re = 2 \times 10^6$ and $\alpha = 14$ deg.

Typically, four layers (including the input and output layers) and 128 neurons (total) were employed with a sigmoid activation function. During the training stage, a reduction in loss function by a factor of 0.0001 was used as an early stopping criterion.

To train the neural network, fivefold cross validation is performed. The data are randomly partitioned into five equally sized groups. One of those groups is used as a validation group, and the rest are used for training, thus resulting in a total of five test sets (Table 1). In the following section, the results of the cross-validation procedure will be presented.

V. Results

The utility of the data-driven framework is demonstrated in three wind turbine airfoils with varying thicknesses: 1) S805, 2) S809, and 3) S814 (Fig. 6). This specific set was chosen for this work because of the availability (in the open literature, [53–55]) of the lift and drag polar from low angles of attack through incipient and massive separation and for multiple Reynolds numbers: $Re \in \{1 \times 10^6, 2 \times 10^6, 3 \times 10^6\}$. Additionally, detailed pressure measurements are available at some test points.

Full-field inversion was performed for each airfoil at different combinations of angles of attack and Reynolds number. In all the cases, inversion was based on just the lift coefficient. For the S809 airfoil at $Re = 2 \times 10^6$, the lift-based inversion was compared to the pressure-based inversion as shown in Fig. 2. Inversion was followed by employing the neural network to reconstruct model corrections. Neural network training was based on the S814 airfoil data at Reynolds number of 1 and 2 million, which we will refer to as dataset P. This dataset was chosen because adverse pressure

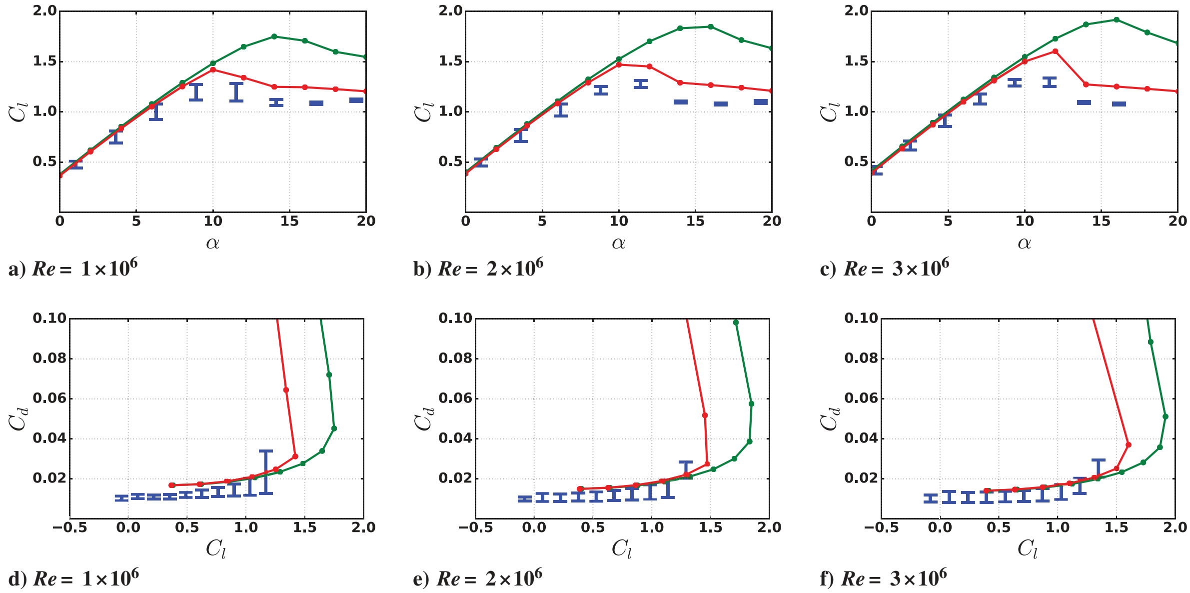

Fig. 10 Pressure and skin friction for a representative case using grids of different spatial resolutions.

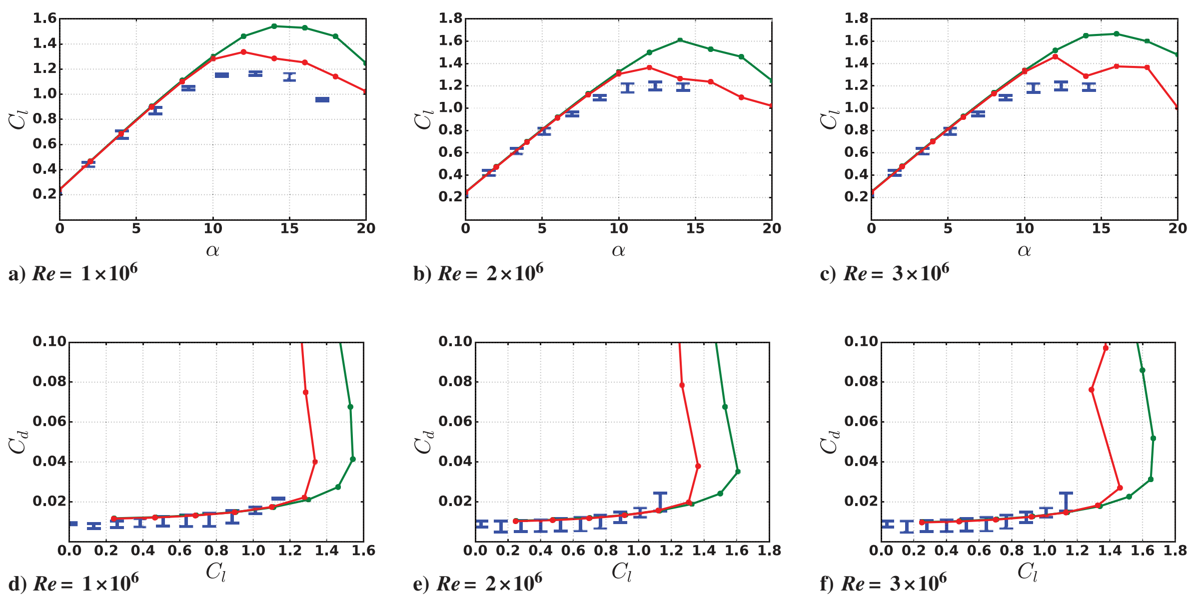

Fig. 11 NN-augmented SA prediction for S805 airfoil using dataset P: experiment (blue), base SA (green), and neural network (red).

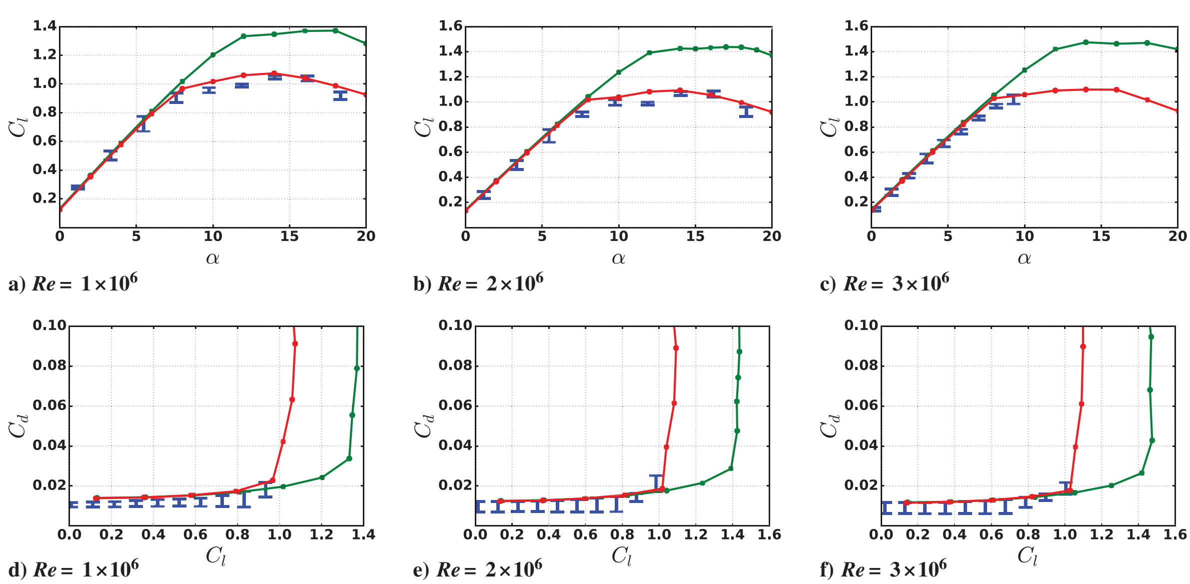

Fig. 12 NN-augmented SA prediction for S809 airfoil using dataset P: experiment (blue), base SA (green), and neural network (red).

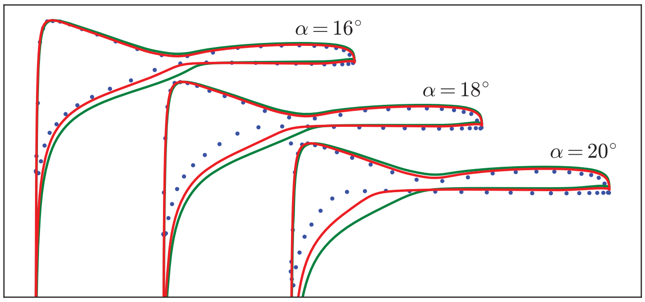

Fig. 13 Surface pressure coefficient for S809 airfoil at $Re = 2 \times 10^6$ and $\alpha = \{16\ \mathrm{deg}, 18\ \mathrm{deg}, 20\ \mathrm{deg}\}$. Refer to Fig. 8c for legend. (Not to scale.).

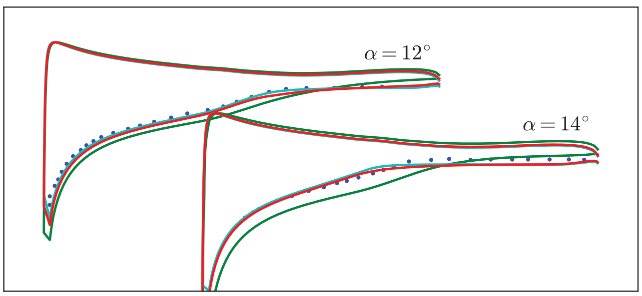

Fig. 14 Surface pressure coefficient for S805 airfoil at $Re = 1 \times 10^6$ and $\alpha = \{12\ \mathrm{deg}, 14\ \mathrm{deg}\}$. Refer to Fig. 8c for the legend.

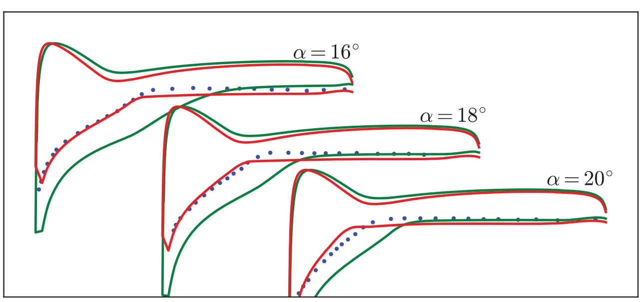

Fig. 15 Surface pressure coefficient for S814 airfoil at $Re = 1.5 \times 10^6$ and $\alpha = \{16\ \mathrm{deg}, 18\ \mathrm{deg}, 20\ \mathrm{deg}\}$. Refer to Fig. 8c for the legend.

gradients are the largest. Figure 7 shows the testing and training results on dataset P.

As schematized in Fig. 1, the mapping $\beta(\eta)$ built during the training process is queried for input features $\hat{\eta}$ at every iteration of the flow solver to obtain outputs $\hat{\beta}$ that are embedded into the predictive model. This process is repeated until convergence. Thus, consistency is enforced between the underlying flowfield and the model augmentations. Later in this section, ensemble comparisons based on different training datasets will also be shown.

A. Predictions

The effectiveness of the inversion and learning is apparent in Figs. 8 and 9, where the predictions based on model P are compared to the ideal scenario of direct inference on the S809 airfoil based on experimental data. It has to be mentioned that the training dataset was based on assimilating lift information only.

Figure 10 shows the lift and drag coefficients for all Reynolds numbers for the S814 airfoil, including $Re = 3 \times 10^6$, which was not used in the training set. Clearly, significant improvement in stall prediction is evident in the lift prediction. As a consequence, the drag rise is predicted to occur at lower angles of attack than in the baseline model, which is a trend that is qualitatively correct. Furthermore, there is no evidence of deterioration of accuracy in the low angle-of-attack regions, where the original model is already accurate. The model performs equally well for airfoil shapes not used in the training set, i.e., S805 and S809 (Figs. 11 and 12).

The improvement in the quality of the predictions is further emphasized in Figs. 13–15, in which pressure predictions are shown for the S809, S805, and S814 airfoils. These results confirm that the NN-augmented model offers considerable predictive improvements in surface pressure distributions.

Figure 16 shows the base SA and the NN augmented SA solutions for two different grid resolutions. The solutions using both the models suggest that the variability in the solution between the two grids is much smaller than the corrections introduced by the data augmentation.

B. Predictive Variability

It is desirable that any new modifications introduced into a turbulence model do not affect the solution to problems for which the base model is accurate. The results suggest that the NN-augmented SA model satisfies this requirement. Figure 17 showcases this feature for the S809 airfoil at a Reynolds number of 2×10^6. The predicted surface pressure using neural networks trained on different datasets listed in Table 2 is shown in red lines. Clearly, model augmentations show variability, as is apparent in Figs. 17b and 17c. Overall, the neural network-augmented models are more accurate than the base SA model for all the cases; more important, none of the NN-augmented predictions diverge from the base SA model at $\alpha = 0$ deg. Although this ensemble approach does not qualify as a formal uncertainty quantification technique, it is nevertheless a useful test to ascertain the sensitivity of the model output to the training set. If significant variabilities are revealed in the model predictions, it serves as a warning to the user that models may be operating far from conditions in which they were trained.

Furthermore, Fig. 17 shows that the quality of the NN-augmented model is sensitive to the selection of the training data. In this work, the best model, which is model "P", is selected by exploring several combinations of the datasets. This observation is subjected to the

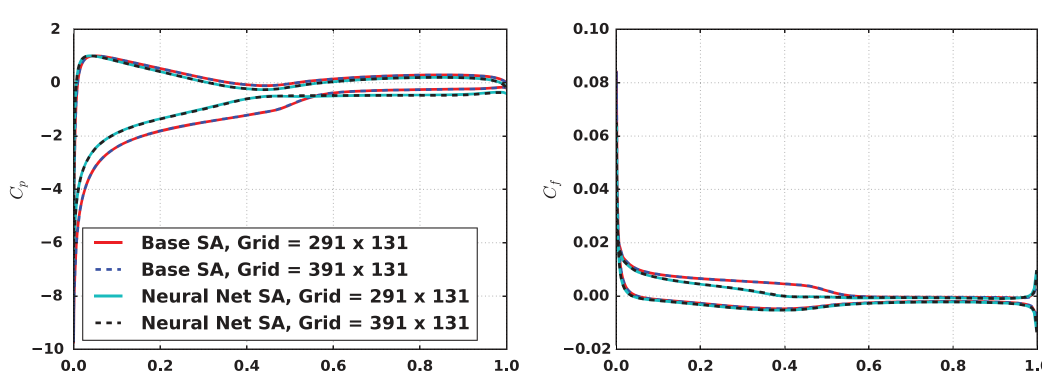

a) C_p b) C_f

Fig. 16 Pressure and skin friction (using dataset P) for S809 airfoil at $Re = 2 \times 10^6$ and $\alpha = 14$ deg using grids of different spatial resolutions. Solutions of both the base SA model and the neural-network-augmented SA are grid converged.

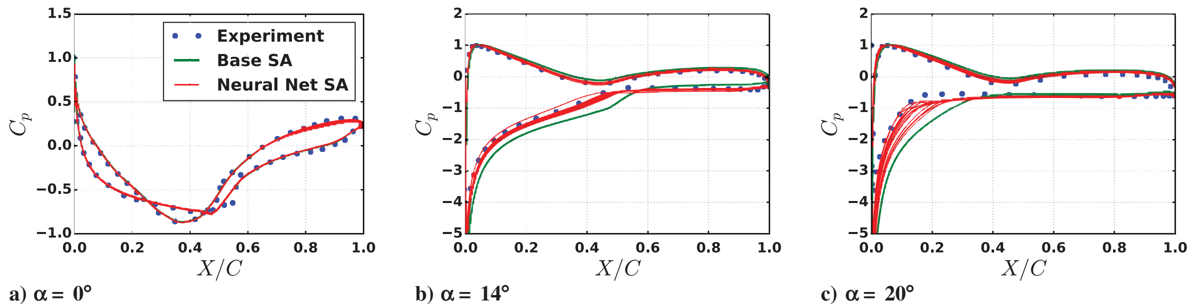

Fig. 17 Predicted pressure coefficients for S809 at $Re = 2 \times 10^6$ using eight different NN-based models, listed in Table 2.

uncertainty involved with the intermediate steps (feature selection, machine-learning algorithm, etc.).

C. Portability and Convergence

The entire modeling framework was developed and tested on ADTURNS, which is a structured finite volume flow solver augmented with adjoint optimization and neural networks. To demonstrate the portability of this approach, the NN-augmented SA model based on dataset P is implemented into AcuSolve, which is a commercially available unstructured flow solver based on the Galerkin/least-squares (GLS) stabilized finite element method [56,57]. Although ADTURNS implements nondimensionalized RANS equations, AcuSolve implements the dimensional form of RANS equations. Therefore, developing the neural network model based on a feature set consisting of locally nondimensional flow variables, as presented in this work, is essential for portability across flow solvers.

AcuSolve is a general-purpose solver that is used in a wide variety of applications such as wind power, automotive, offshore engineering, electronics cooling, chemical mixing, biomedical, consumer products, national laboratories, and academic research [58–62]. The GLS formulation with linear shape functions provides second-order accuracy for spatial discretization of all variables and uses tightly controlled numerical diffusion operators to obtain stability and maintain accuracy. The semidiscrete generalized-alpha method is used to integrate the equations implicitly in time for steady-state and transient simulations [63]. The resulting system of equations is solved as a fully coupled pressure/velocity matrix system using a preconditioned iterative linear solver.

Figure 18 shows lift and drag coefficient predictions from AcuSolve for the S809 airfoil at three Reynolds numbers. The NN augmentation shows significant improvement in predictions, and its effectiveness is comparable to that observed in the ADTURNS solver framework. It should be noted that AcuSolve uses a variation of the SA model that corrects for the rotation and the curvature effects. These corrections are not used in the ADTURNS code; therefore, the solutions from these two codes are not expected to be identical, even for the baseline model.

Figure 19 shows the rate of convergence for the base SA and the NN-augmented SA for the sample problem. The initial condition was taken to be uniform freestream for all the runs. The NN-augmented model displays comparable convergence characteristics to the baseline model, thus demonstrating the portability of the approach. Additional overhead exists in passing the features $\boldsymbol{\eta}$ to the NN and obtaining β at grid locations. This was confirmed to add less than 10% of the additional compute time compared to the baseline calculation.

Table 2 List of datasets used to study the impact of variability of the training[a]

Model label	Training data
P	S814 at $\boldsymbol{Re} = 1 \times 10^6, 2 \times 10^6$
1	S805 at $Re = 1 \times 10^6$
2	S805 at $Re = 2 \times 10^6$
3	S809 at $Re = 1 \times 10^6$
4	S809 at $Re = 2 \times 10^6$
5	S805 at $Re = 1 \times 10^6, 2 \times 10^6$
6	S809 at $Re = 1 \times 10^6, 2 \times 10^6$
7	S805, S809, and S814 at $Re = 1 \times 10^6, 2 \times 10^6$

[a]The main predictive model is constructed based on dataset P. Note that $Re = 3 \times 10^6$ is not included in any of the datasets.

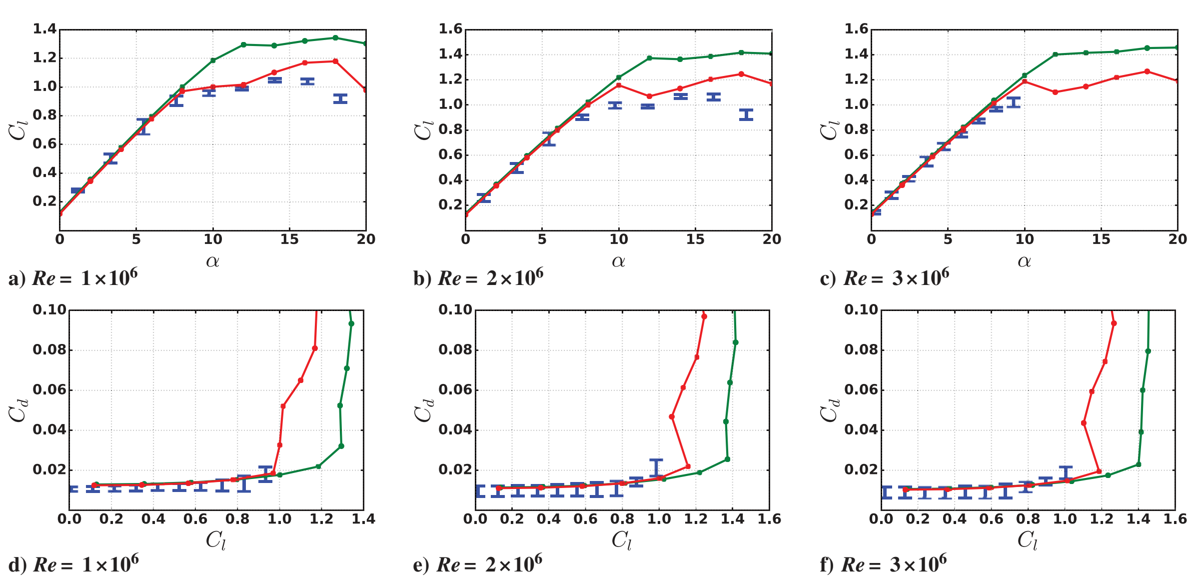

Fig. 18 NN-augmented SA prediction using AcuSolve for S809 airfoil using dataset P: experiment (blue), base SA (green), and neural network (red).

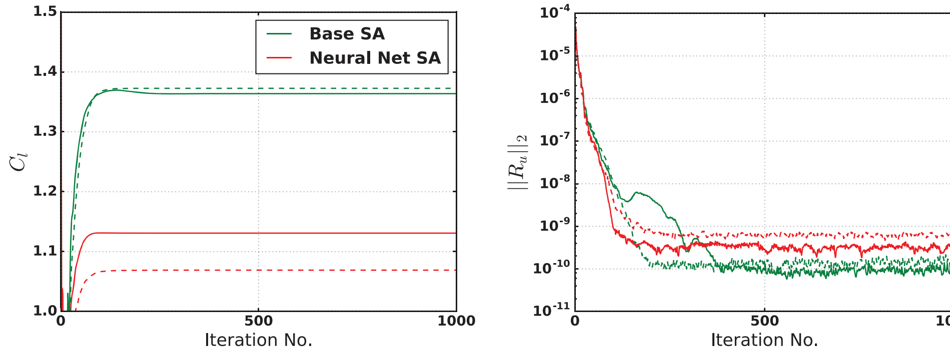

a) Lift coefficient

b) L2 norm of solver residual

Fig. 19 AcuSolve's convergence history for S809 airfoil at $Re = 2 \times 10^6$, $\alpha = 12$ deg (dashed lines), and $\alpha = 14$ deg (solid lines).

VI. Conclusions

A data-driven framework comprising full-field inversion and machine learning was used to develop predictive capabilities for the modeling of turbulent separated flows over airfoils. This framework was embedded in a traditional RANS solver to improve the applicability of the Spalart–Allmaras turbulence model to strong adverse pressure gradients present in flow past airfoils prestall and poststall. With a view toward assimilating sparse data from a wide range of flows, the inversion process was formulated as an optimization problem to minimize the difference between the experimentally measured lift coefficient and the model output. In contrast to parametric inversion, the turbulence model discrepancy was inferred as a field (i.e., at every grid point in the solution domain). The resulting model-correction function was then reconstructed using an artificial neural network as a function of locally nondimensional flow quantities such as the ratio of eddy to kinematic viscosity and the vorticity to strain-rate magnitude.

During the predictive process, the neural network (NN) was queried at every iteration of the flow solver to obtain model corrections that are embedded into the predictive model. The resulting data-augmented turbulence model was then used for predictive simulations of airfoils and flow conditions that were not part of the neural network training. Extensive tests were made, and the following conclusions were observed:

1) The data-assisted Spalart–Allmaras model showed significant improvement over the baseline model in predicting lift and drag coefficients, and stall onset angles.

2) The model predictions were confirmed to be significantly improved for airfoil shapes and flow conditions that were not part of the training set.

3) No deterioration of accuracy was noticed in situations (low angles of attack) in which the original model was accurate.

4) Though the inference process used only the lift-coefficient data, the NN-augmented model was demonstrated to provide considerable predictive improvements of surface pressure distributions. This reinforced confidence that the procedure did not overfit the model to the lift data and that predictive improvements were realized for the right reasons.

5) An ensemble of predictions based on different training sets was used to assess the sensitivity of the model outputs to the training data. Although there was expected variability in the results, the model augmentations brought predictions closer to the experimental results for all training sets.

6) Solver convergence was assessed, and the cost overhead for the NN augmentations was observed to be minimal.

7) Portability of the approach was demonstrated by generating the data-assisted SA model using a structured finite volume solver and then using it in AcuSolve, which is a a commercial, unstructured finite element solver. The predictive improvements were confirmed to be preserved across both solvers.

Although the present work was focused on demonstrating the potential of data-driven approaches based on field inference and learning, much work remains to be done in developing turbulence models for application in more general settings. In such situations, the ensemble of datasets (as in Fig. 17) may be used as a rule of thumb to indicate the variability of the machine-learning-augmented model. However, a more formal uncertainty quantification approach that takes into account the uncertainty in the data, variability of the training process, and confidence in the baseline model may be desirable. A simplified form of such an approach has been proposed (and demonstrated for much simpler problems) in [28].

One immediate avenue to extend this effort is to target specific engineering applications where current computational fluid dynamics predictions are unsatisfactory. In this situation, customized modeling augmentations can be generated to improve predictions. Furthermore, industrial applications tend to be focused on a class of problems (for example, wind turbine rotors or turbomachinery blades) in which experimental data may be available in some regimes. These types of problems are most amenable to data-augmented modeling.

The philosophy and formalisms employed in this work are of a general nature and are not restricted to the type of model or the type of model discrepancy that is addressed. The inversion/learning/embedding procedure can be applied, for instance, to address discrepancies in the Reynolds stress anisotropy [21,32]. In such endeavors, it would be critical to ensure that the model augmentations 1) include available experimental data (as one will always be hard pressed to obtain large-eddy simulation and direct numerical simulation data in regimes of interest), 2) do not influence regions of the flow that are adequately represented by the baseline model (near-wall region in thin boundary layers), and 3) do not degrade the convergence properties of the solver. There is much to be gained by carefully exploring a broader set of input features [24,32] and alternative machine-learning methods [23,49]. Finally, respecting realizability limits [18,32] and invariance properties [31] will be necessary to constrain the model, especially when the model is operating in an extrapolatory mode.

Appendix A: Discrete Adjoint Method for Field Inversion

The formulation and application of field inversion techniques to turbulence modeling problems was provided in [28,29]. A brief description is presented herein for completeness. The optimization procedure to minimize Eq. (4) or Eq. (5) uses a gradient-based quasi-Newton method employing the limited memory Broyden–Fletcher–Goldfarb–Shanno algorithm [64]. Because the optimization problem is extremely high-dimensional (as the number of parameters equals the number of control volumes N_m), an adjoint approach is required to efficiently compute gradients. In the adjoint technique, given an objective function $\mathcal{J}$ that we wish to minimize, the total derivative with respect to the parameter vector

$$\beta = \{\beta(x_1), \beta(x_2), \ldots, \beta(x_{N_m})\}^T$$

is given by

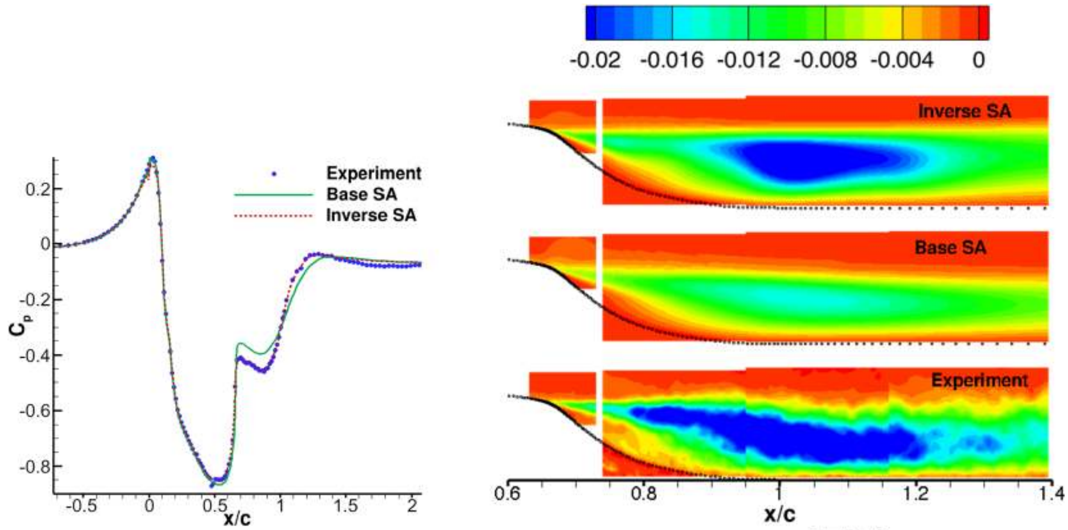

a) Wall pressure coefficient   b) Reynolds shear-stress contours $\overline{u_1' u_2'}/U_\infty^2$

Fig. C1 Application of inverse modeling to separated flow over a smooth surface.

$$\frac{\mathrm{d}\mathcal{J}}{\mathrm{d}\beta} = \frac{\partial \mathcal{J}}{\partial \beta} + \boldsymbol{\psi}^T \frac{\partial \boldsymbol{R}}{\partial \beta} \tag{A1}$$

In the preceding equation,** $\boldsymbol{R}$ represents the governing equations and $\boldsymbol{\psi}$ is the vector of adjoint variables, which is determined by

$$\left[\frac{\partial \boldsymbol{R}}{\partial \boldsymbol{U}}\right]^T \boldsymbol{\psi} = -\left[\frac{\partial \mathcal{J}}{\partial \boldsymbol{U}}\right]^T \tag{A2}$$

The partial derivatives in Eq. (A2) are calculated using the tapenade [65] tool for automatic differentiation, and the system is solved using pseudotime stepping. Because β is explicitly present only as a multiplier to the production term $\boldsymbol{P}$, the expression for the gradient is given by

$$\frac{\mathrm{d}\mathcal{J}}{\mathrm{d}\beta} = \frac{\partial \mathcal{J}}{\partial \beta} - \boldsymbol{\psi}_{\tilde{\nu}}^T \boldsymbol{P} \tag{A3}$$

where $\boldsymbol{\psi}_{\tilde{\nu}}$ represents the adjoint variable corresponding to the working variable of the SA model.

Appendix B: Spalart–Allmaras Model

The one-equation Spalart–Allmaras turbulence model [37] is used for the work presented in this paper. The S-A model solves for the modified eddy viscosity $\tilde{\nu}$, which relates to the kinematic eddy viscosity ν_t as follows:

$$\nu_t = \tilde{\nu} f_{v1}; \qquad f_{v1} = \frac{\chi^3}{\chi^3 + c_{v1}^3}; \qquad \chi = \frac{\tilde{\nu}}{\nu} \tag{B1}$$

The governing equation of the S-A model without the trip terms is given by the following:

$$\frac{\mathrm{D}\tilde{\nu}}{\mathrm{D}t} = P - D + \frac{1}{\sigma}[\nabla \cdot ((\nu + \tilde{\nu})\nabla\tilde{\nu}) + c_{b2}(\nabla\tilde{\nu})^2], \tag{B2}$$

where P and D are the production and destruction terms of $\tilde{\nu}$ given by the following:

$$P = c_{b1}\tilde{\Omega}\tilde{\nu} \quad \text{and} \quad D = c_{w1} f_w \left[\frac{\tilde{\nu}}{d}\right]^2 \tag{B3}$$

$\tilde{\Omega}$ is a function of the vorticity magnitude Ω and is defined as follows:

$$\tilde{\Omega} = \Omega + \frac{\tilde{\nu}}{\kappa^2 d^2} f_{v2}, \qquad f_{v2} = 1 - \frac{\chi}{1 + \chi f_{v1}} \tag{B4}$$

The function f_w is defined as follows:

$$f_w = g\left[\frac{1 + c_{w3}^6}{g^6 + c_{w3}^6}\right]^{1/6}, \quad g = r + c_{w2}(r^6 - r), \qquad r = \frac{\tilde{\nu}}{\tilde{\Omega}\kappa^2 d^2} \tag{B5}$$

The model constants are $c_{b1} = 0.1355$, $\sigma = 2/3$, $c_{b2} = 0.622$, $\kappa = 0.41$, $c_{w1} = c_{b1}/\kappa^2 + (1 + c_{b2})/\sigma$, $c_{w2} = 0.622$, $c_{w3} = 2.0$, and $c_{v1} = 7.1$. Freestream boundary is set to fully turbulent with $\tilde{\nu}/\nu_\infty = 3$, and, $\tilde{\nu}$ is set to zero at no-slip walls.

Appendix C: Inverse Modeling for Separated Flows

As mentioned in Sec. III, inverse modeling was used to provide quantitative information about the model discrepancy. Machine-learning-based augmentations are based on inverse fields that were generated using lift data. This was confirmed to also result in good surface pressure predictions. To assess the generality of the procedure and its impact on other field quantities, the inverse problem was applied to a NASA benchmark test [66] (Fig. C1), which involved separated flow over a smooth hump. In this problem, $\beta(x, y)$ was inferred with the objective of matching the wall pressure distribution in the region $0.5 \le x/c \le 1.5$. Even though the objective function was only taken to be the surface pressure, improvement was seen in the Reynolds stress predictions (Fig. C1c). As a consequence of the overall improvement in the field solution, the predicted length of the separation bubble was found be 15% more accurate as compared to the baseline solution. Results could be improved by considering more information from the experiment [29], but this exercise offered further evidence that, for separated flows, pressure data were valuable in inferring model discrepancy.

Acknowledgments

This work was funded by the NASA Aeronautics Research Institute under the Leading Edge Aeronautics Research for NASA program (monitors: Koushik Datta and Gary Coleman). A portion of

**$\boldsymbol{R}$ and $\boldsymbol{\psi}$ are of dimension $5N_m$.

this work was performed as part of a summer internship program at Altair Engineering, Inc. Shaowu Pan assisted with the machine learning. The authors acknowledge insightful discussions with Brendan Tracey, Paul Durbin, and Juan Alonso. Computing resources were provided by the NSF via grant 1531752 MRI: Acquisition of Conflux, A Novel Platform for Data-Driven Computational Physics (Tech. Monitor: Ed Walker).

References

[1] Slotnick, J., Khodadoust, J., Alonso, J., Darmofal, D., Gropp, W., Lurie, E., and Mavriplis, D., "CFD Vision 2030 Study: A Path to Revolutionary Computational Aerosciences," NASA Langley Research Center, NASA/CR 2014-218178, Hampton, VA, 2013.

[2] Gerolymos, G. A., Sauret, E., and Vallet, I., "Contribution to Single-Point Closure Reynolds-Stress Modelling of Inhomogeneous Flow," *Theoretical and Computational Fluid Dynamics*, Vol. 17, Nos. 5–6, 2004, pp. 407–431.
doi:10.1007/s00162-004-0109-5

[3] Younis, B., Gatski, T., and Speziale, C. G., "Towards a Rational Model for the Triple Velocity Correlations of Turbulence," *Proceedings of the Royal Society of London, Series A: Mathematical, Physical and Engineering Sciences*, Vol. 456, No. 1996, 2000, pp. 909–920.
doi:10.1098/rspa.2000.0542

[4] Poroseva, S., and Murman, S. M., "Velocity/Pressure-Gradient Correlations in a FORANS Approach to Turbulence Modeling," *44th AIAA Fluid Dynamics Conference, AIAA Aviation*, AIAA Paper 2014-2207, June 2014.

[5] Durbin, P. A., "Near-Wall Turbulence Closure Modeling Without Damping Functions," *Theoretical and Computational Fluid Dynamics*, Vol. 3, No. 1, 1991, pp. 1–13.

[6] Durbin, P., "A Reynolds Stress Model for Near-Wall Turbulence," *Journal of Fluid Mechanics*, Vol. 249, April 1993, pp. 465–498.
doi:10.1017/S0022112093001259

[7] Milano, M., and Koumoutsakos, P., "Neural Network Modeling for Near Wall Turbulent Flow," *Journal of Computational Physics*, Vol. 182, No. 1, 2002, pp. 1–26.
doi:10.1006/jcph.2002.7146

[8] Marusic, I., Candler, G., Interrante, V., Subbareddy, P., and Moss, A., "Real Time Feature Extraction for the Analysis of Turbulent Flows," *Data Mining for Scientific and Engineering Applications*, Vol. 2, 2001, pp. 223–238.
doi:10.1007/978-1-4615-1733-7_13

[9] Yarlanki, S., Rajendran, B., and Hamann, H., "Estimation of Turbulence Closure Coefficients for Data Centers Using Machine Learning Algorithms," *13th Intersociety Conference on Thermal and Thermomechanical Phenomena in Electronic Systems*, IEEE Publ., Piscataway, NJ, 2012, pp. 38–42.
doi:10.1109/ITHERM.2012.6231411

[10] Kato, H., and Obayashi, S., "Data Assimilation for Turbulent Flows," *16th AIAA Non-Deterministic Approaches Conference, AIAA SciTech*, AIAA Paper 2014-1177, Jan. 2014.

[11] Edeling, W., Cinnella, P., Dwight, R. P., and Bijl, H., "Bayesian Estimates of Parameter Variability in the $k-\varepsilon$ Turbulence Model," *Journal of Computational Physics*, Vol. 258, Feb. 2014, pp. 73–94.
doi:10.1016/j.jcp.2013.10.027

[12] Ray, J., Lefantzi, S., Arunajatesan, S., and DeChant, L. J., "Bayesian Calibration of a RANS Model with a Complex Response Surface—A Case Study with Jet-in-Crossflow Configuration," *45th AIAA Fluid Dynamics Conference*, AIAA Paper 2015-2784, June 2015.

[13] Cheung, S. H., Oliver, T. A., Prudencio, E. E., Prudhomme, S., and Moser, R. D., "Bayesian Uncertainty Analysis with Applications to Turbulence Modeling," *Reliability Engineering and System Safety*, Vol. 96, No. 9, 2011, pp. 1137–1149.
doi:10.1016/j.ress.2010.09.013

[14] Oliver, T. A., and Moser, R. D., "Bayesian Uncertainty Quantification Applied to RANS Turbulence Models," *Journal of Physics: Conference Series*, Vol. 318, No. 4, 2011, Paper 042032.

[15] Cheung, S. H., and Beck, J., "New Bayesian Updating Methodology for Model Validation and Robust Predictions Based on Data from Hierarchical Subsystem Tests," Earthquake Engineering Research Lab., California Inst. of Technology, Rept. CaltechEERL:EERL-2008-04, Pasadena, CA, Jan. 2009.

[16] Dow, E., and Wang, Q., "Uncertainty Quantification of Structural Uncertainties in RANS Simulations of Complex Flows," *20th AIAA Computational Fluid Dynamics Conference*, AIAA Paper 2011-3865, June 2011.

[17] Dow, E., and Wang, Q., "Quantification of Structural Uncertainties in the $k-\omega$ Turbulence Model," *52nd AIAA/ASME/ASCE/AHS/ASC Structures, Structural Dynamics and Materials Conference*, AIAA Paper 2011-1762, April 2011.

[18] Emory, M., Pecnik, R., and Iaccarino, G., "Modeling Structural Uncertainties in Reynolds-Averaged Computations of Shock/Boundary Layer Interactions," *49th AIAA Aerospace Sciences Meeting including the New Horizons Forum and Aerospace Exposition*, AIAA Paper 2011-0479, Jan. 2011.

[19] Gorle, C., Emory, M., and Iaccarino, G., "RANS Modeling of Turbulent Mixing for a Jet in Supersonic Cross Flow: Model Evaluation and Uncertainty Quantification," *Proceedings of the Seventh International Symposium on Turbulence, Heat and Mass Transfer (ICHMT Digital Library Online, Palermo, Italy)*, International Centre for Heat and Mass Transfer Digital Library, Begell House Publ., 2012.
doi:10.1615/ICHMT.2012.ProcSevIntSympTurbHeatTransfPal.1830

[20] Emory, M., Larsson, J., and Iaccarino, G., "Modeling of Structural Uncertainties in Reynolds-Averaged Navier-Stokes Closures," *Physics of Fluids*, Vol. 25, No. 11, 2013, Paper 110822.

[21] Tracey, B., Duraisamy, K., and Alonso, J., "Application of Supervised Learning to Quantify Uncertainties in Turbulence and Combustion Modeling," *51st AIAA Aerospace Sciences Meeting Including the New Horizons Forum and Aerospace Exposition Grapevine*, AIAA Paper 2013-0259, Jan. 2013.

[22] Xiao, H., Wu, J.-L., Wang, J.-X., Sun, R., and Roy, C. J., "Quantifying and Reducing Model-Form Uncertainties in Reynolds-Averaged Navier-Stokes Equations: A Data-Driven, Physics-Informed Bayesian Approach," *Journal of Computational Physics*, Vol. 324, 2016, pp. 115–136.
doi:10.1016/j.jcp.2016.07.038

[23] Weatheritt, J., "The Development of Data Driven Approaches to Further Turbulence Closures," Ph.D. Thesis, Univ. of Southampton, Southampton, England, U.K., 2015.

[24] Ling, J., and Templeton, J., "Evaluation of Machine Learning Algorithms for Prediction of Regions of High Reynolds Averaged Navier Stokes Uncertainty," *Physics of Fluids*, Vol. 27, No. 8, 2015, Paper 085103.
doi:10.1063/1.4927765

[25] King, R., Hamlington, P. E., and Dahm, W., "Autonomic Subgrid-Scale Closure for Large Eddy Simulations," *53rd AIAA Aerospace Sciences Meeting, AIAA SciTech*, AIAA Paper 2015-1285, Jan. 2015.

[26] Duraisamy, K., Zhang, Z. J., and Singh, A. P., "New Approaches in Turbulence and Transition Modeling Using Data-driven Techniques," *53rd AIAA Aerospace Sciences Meeting, AIAA SciTech*, AIAA Paper 2015-1284, Jan. 2015.

[27] Tracey, B. D., Duraisamy, K., and Alonso, J. J., "A Machine Learning Strategy to Assist Turbulence Model Development," *53rd AIAA Aerospace Sciences Meeting, AIAA SciTech*, AIAA Paper 2015-1287, Jan. 2015.

[28] Parish, E. J., and Duraisamy, K., "A Paradigm for Data-Driven Predictive Modeling Using Field Inversion and Machine Learning," *Journal of Computational Physics*, Vol. 305, Jan. 2016, pp. 758–774.
doi:10.1016/j.jcp.2015.11.012

[29] Singh, A. P., and Duraisamy, K., "Using Field Inversion to Quantify Functional Errors in Turbulence Closures," *Physics of Fluids*, Vol. 28, No. 4, 2016, Paper 045110.
doi:10.1063/1.4947045

[30] Ling, J., Kurzawski, A., and Templeton, J., "Reynolds Averaged Turbulence Modelling Using Deep Neural Networks with Embedded Invariance," *Journal of Fluid Mechanics*, Vol. 807, Nov. 2016, pp. 155–166.
doi:10.1017/jfm.2016.615

[31] Ling, J., Jones, R., and Templeton, J., "Machine Learning Strategies for Systems with Invariance Properties," *Journal of Computational Physics*, Vol. 318, Aug. 2016, pp. 22–35.
doi:10.1016/j.jcp.2016.05.003

[32] Wang, J.-X., Wu, J.-L., and Xiao, H., "Physics Informed Machine Learning Approach for Reconstructing Reynolds Stress Modeling Discrepancies Based on DNS Data," *Physical Review Fluids*, Vol. 2, No. 3, 2017, pp. 1–22.
doi:10.1103/PhysRevFluids.2.034603

[33] Celic, A., and Hirschel, E. H., "Comparison of Eddy-Viscosity Turbulence Models in Flows with Adverse Pressure Gradient," *AIAA Journal*, Vol. 44, No. 10, 2006, pp. 2156–2169.
doi:10.2514/1.14902

[34] Menter, F. R., "Two-Equation Eddy-Viscosity Turbulence Models for Engineering Applications," *AIAA Journal*, Vol. 32, No. 8, 1994, pp. 1598–1605.
doi:10.2514/3.12149

[35] Wilcox, D. C., "Formulation of the $k-\omega$ Turbulence Model Revisited," *AIAA Journal*, Vol. 46, No. 11, 2008, pp. 2823–2838. doi:10.2514/1.36541

[36] Rung, T., Bunge, U., Schatz, M., and Thiele, F., "Restatement of the Spalart–Allmaras Eddy-Viscosity Model in Strain-Adaptive Formulation," *AIAA Journal*, Vol. 41, No. 7, 2003, pp. 1396–1399. doi:10.2514/2.2089

[37] Spalart, P., and Allmaras, S., "A One-Equation Turbulence Model for Aerodynamic Flows," *30th Aerospace Sciences Meeting and Exhibit*, AIAA Paper 1992-0439, Jan. 1992.

[38] Duraisamy, K., McCroskey, W. J., and Baeder, J. D., "Analysis of Wind Tunnel Wall Interference Effects on Subsonic Unsteady Airfoil Flows," *Journal of Aircraft*, Vol. 44, No. 5, 2007, pp. 1683–1690. doi:10.2514/1.28143

[39] Bremseth, J., and Duraisamy, K., "Computational Analysis of Vertical Axis Wind Turbine Arrays," *Theoretical and Computational Fluid Dynamics*, Vol. 30, No. 5, 2016, pp. 387–401. doi:10.1007/s00162-016-0384-y

[40] Lakshminarayan, V. K., and Duraisamy, K., "Adjoint-Based Estimation and Control of Spatial, Temporal and Stochastic Approximation Errors in Unsteady Flow Simulations," *Computers and Fluids*, Vol. 121, Oct. 2015, pp. 180–191. doi:10.1016/j.compfluid.2015.08.020

[41] Van Leer, B., "Towards the Ultimate Conservative Difference Scheme. V. A Second-Order Sequel to Godunov's Method," *Journal of Computational Physics*, Vol. 32, No. 1, 1979, pp. 101–136. doi:10.1016/0021-9991(79)90145-1

[42] Roe, P. L., "Approximate Riemann Solvers, Parameter Vectors, and Difference Schemes," *Journal of Computational Physics*, Vol. 43, No. 2, 1981, pp. 357–372. doi:10.1016/0021-9991(81)90128-5

[43] Pulliam, T. H., and Chaussee, D., "A Diagonal Form of an Implicit Approximate-Factorization Algorithm," *Journal of Computational Physics*, Vol. 39, No. 2, 1981, pp. 347–363. doi:10.1016/0021-9991(81)90156-X

[44] Giles, M. B., and Pierce, N. A., "An Introduction to the Adjoint Approach to Design," *Flow, Turbulence and Combustion*, Vol. 65, Nos. 3–4, 2000, pp. 393–415. doi:10.1023/A:1011430410075

[45] Bishop, C. M., "Training with Noise is Equivalent to Tikhonov Regularization," *Neural Computation*, Vol. 7, No. 1, 1995, pp. 108–116. doi:10.1162/neco.1995.7.1.108

[46] Rumsey, C. L., and Ying, S. X., "Prediction of High Lift: Review of Present CFD Capability," *Progress in Aerospace Sciences*, Vol. 38, No. 2, 2002, pp. 145–180. doi:10.1016/S0376-0421(02)00003-9

[47] Spalart, P. R., Deck, S., Shur, M. L., Squires, K. D., Strelets, M. K., and Travin, A., "A New Version of Detached-Eddy Simulation, Resistant to Ambiguous Grid Densities," *Theoretical and Computational Fluid Dynamics*, Vol. 20, No. 3, 2006, pp. 181–195. doi:10.1007/s00162-006-0015-0

[48] Zhang, Z. J., and Duraisamy, K., "Machine Learning Methods for Data-Driven Turbulence Modeling," *22nd AIAA Computational Fluid Dynamics Conference, AIAA Aviation*, AIAA Paper 2015-2460, June 2015.

[49] Zhang, Z., Duraisamy, K., and Gumerov, N., "Efficient Multiscale Gaussian Process Regression Using Hierarchical Clustering," 2016.

[50] Bishop, C. M., *Pattern Recognition and Machine Learning*, 1st ed., Springer–Verlag, New York, 2006, pp. 225–284.

[51] Nissen, S., "Implementation of a Fast Artificial Neural Network Library (Fann)," Dept. of Computer Science, Univ. of Copenhagen, Copenhagen, Denmark, 2003, http://leenissen.dk/fann [retrieved 22 March 2017].

[52] Igel, C., and Hüsken, M., "Empirical Evaluation of the Improved Rprop Learning Algorithms," *Neurocomputing*, Vol. 50, Jan. 2003, pp. 105–123. doi:10.1016/S0925-2312(01)00700-7

[53] Somers, D. M., "Design and Experimental Results for the S805 Airfoil," National Renewable Energy Lab. Rept. NREL/SR 440-6917, Golden, CO, 1997.

[54] Somers, D. M., "Design and Experimental Results for the S809 Airfoil," Renewable Energy Lab. Rept. NREL/SR 440-6918, Golden, CO, 1997.

[55] Somers, D. M., "Design and Experimental Results for the S814 Airfoil," Renewable Energy Lab. Rept. NREL/SR 440-6919, Golden, CO, 1997.

[56] Hughes, T. J. R., France, L. P., and Hulbert, G. M., "A New Finite Element Formulation for Computational Fluid Dynamics. VIII. The Galerkin/Least-Squares Method for Advective-Diffusive Equations," *Computer Methods in Applied Mechanics and Engineering*, Vol. 73, No. 2, 1989, pp. 173–189. doi:10.1016/0045-7825(89)90111-4

[57] Shakib, F., Hughes, T. J. R., and Johan, Z., "A New Finite Element Formulation for Computational Fluid Dynamics. X. The Compressible Euler and Navier-Stokes Equations," *Computer Methods in Applied Mechanics and Engineering*, Vol. 89, Nos. 1–3, 1991, pp. 141–219. doi:10.1016/0045-7825(91)90041-4

[58] Corson, D. A., Griffith, D. T., Ashwill, T., and Shakib, F., "Investigating Aeroelastic Performance of Multi-Megawatt Wind Turbine Rotors Using CFD," *53rd AIAA/ASME/ASCE/AHS/ASC Structures, Structural Dynamics and Materials Conference*, AIAA Paper 2012-1827, 2012.

[59] Corson, D. A., Zamora, A., and Medida, S., "A Comparative Assessment of Correlation-Based Transition Models for Wind Power Applications," *34th AIAA Applied Aerodynamics Conference*, AIAA Paper 2016-3129, 2016.

[60] Godo, M. N., Corson, D., and Lgensky, S. M., "A Comparative Aerodynamic Study of Commercial Bicycle Wheels Using CFD," *48th AIAA Aerospace Sciences Meeting*, AIAA Paper 2010-1431, 2010.

[61] Lyons, D. C., Peltier, L. J., Zajaczkowski, F. J., and Paterson, E. G., "Assessment of DES Models for Separated Flow From a Hump in a Turbulent Boundary Layer," *Journal of Fluids Engineering*, Vol. 131, No. 11, 2009, Paper 111203. doi:10.1115/1.4000376

[62] Bagwell, T. G., "CFD Simulation of Flow Tones From Grazing Flow Past a Deep Cavity," *Proceedings of 2006 ASME International Mechanical Engineering Congress and Exposition*, American Soc. of Mechanical Engineers Paper 2006-15633, Fairfield, NJ, 2006, pp. 105–114.

[63] Jansen, K. E., Whiting, C. H., and Hulbert, G. M., "A Generalized-Alpha Method for Integrating the Filtered Navier-Stokes Equations with a Stabilized Finite Element Method," *Computer Methods in Applied Mechanics and Engineering*, Vol. 190, Nos. 3–4, 2000, pp. 305–319. doi:10.1016/S0045-7825(00)00203-6

[64] Dennis, J. E., Jr., and Moré, J. J., "Quasi-Newton Methods, Motivation and Theory," *SIAM Review*, Vol. 19, No. 1, 1977, pp. 46–89. doi:10.1137/1019005

[65] Hascoet, L., and Pascual, V., "The Tapenade Automatic Differentiation Tool: Principles, Model, and Specification," *ACM Transactions on Mathematical Software (TOMS)*, Vol. 39, No. 3, 2013, Paper 20. doi:10.1145/2450153

[66] Naughton, J. W., Viken, S. A., and Greenblatt, D., "Skin-Friction Measurements on the NASA Hump Model," *AIAA Journal*, Vol. 44, No. 6, 2006, pp. 1255–1265. doi:10.2514/1.14192

S. Fu
Associate Editor